Supporting Information:

Free-Atom-Like *d* States Beyond the Dilute Limit of Single-Atom Alloys

Andrew S. Rosen,[1,2,3] Sudarshan Vijay,[1,3] Kristin A. Persson[1,4,*]

[1]Department of Materials Science and Engineering, University of California, Berkeley, California 94720, USA
[2]Miller Institute for Basic Research in Science, University of California, Berkeley, Berkeley, California 94720, USA
[3]Materials Science Division, Lawrence Berkeley National Laboratory, Berkeley, California 94720, USA
[4]Molecular Foundry, Lawrence Berkeley National Laboratory, Berkeley, California 94720, USA
[*]E-mail: kapersson@lbl.gov

Contents

Data Availability 2
Methods 2
Screening the Materials Project and Identifying Trends 2
Filtering Process 2
Screening for Localized *d* States 2
Density of States Plots for Bulk Intermetallic Compounds 2
Partial Charge Calculations 3
Surface and Adsorption Energy Calculations 3
Slab Generation and Adsorbate Placement 3
Density Functional Theory Parameters 3
Definitions of the Density of States Features 4
Materials Selection for Surface and Adsorption Energy Calculations 5
Modified Newns-Anderson Model 5
Model Parameters for CO Adsorption in the Modified Newns-Anderson Model 6
Additional Results 7
Metals with Localized *d* States: Partial Charges 7
Metals with Localized *d* States: Structure and Composition 8
Periodic Trends for Select Systems 9
d-band Trends Between the Bulk and Surface 12
d-band Trends Between the Intermetallics and Elementals 13
Charge on the CO Adsorbate 13
CO Adsorption Trends 14
Supporting References 15

Data Availability

The data on the Materials Project can be found at https://materialsproject.org. A summary of the tabulated `VASP` data is stored as a JSON file at the following DOI: 10.5281/zenodo.7098518. The VASP output files are stored on NOMAD[1,2] at the following DOI: 10.17172/NOMAD/2022.11.25-2. The code underlying the effective chemisorption model can be found at https://github.com/sudarshanv01/single-atom-alloys (DOI: 10.5281/zenodo.7358098).

Methods

Screening the Materials Project and Identifying Trends

Filtering Process

For the structures considered in this work, we used the Materials Project Application Programming Interface (API)[3] to identify materials on the Materials Project with available DOS data that can be classified as *d*-block containing intermetallics with localized *d* states. The filtering process that corresponds with Figure 1b is summarized as follows:

- Level 1: All materials on the Materials Project with DOS data.
- Level 2: The subset of structures in Level 1 that have at least two unique elements and all the elements are metals or metalloids, as defined in `Pymatgen`.
- Level 3: The subset of structures in Level 2 that have at least one *d*-block metal, do not contain lanthanoids or actinoids, and are classified as metallic (i.e. has a 0 eV band gap) using the band gap data on the Materials Project.
- Level 4: The subset of structures in Level 3 with localized *d* states for group 3–11 metals. We chose group 3–11 metals, as the transition metals are most commonly considered for catalytic applications. Nonetheless, we note that other elements can also exhibit localized *d* states, such as Zn in Au_2CuZn (mp-864623).
- Level 5: The subset of structures in Level 4 with an energy above hull lower than 0.1 eV/atom using the data on the Materials Project.

Note that some of the intermetallics on the Materials Project are alloys with the disorder removed for the purpose of high-throughput DFT calculations.[4] Nonetheless, all such structures are considered in this work.

Screening for Localized *d* States

The signal processing functions in SciPy[5] were used to identify peaks in the *d*-projected DOS for each unique element in a given structure. A peak was identified based on a height and prominence that are both at least 25% of the maximum value in the *d*-projected DOS and a width of least four data points. Any materials with more than one peak in the element- and *d*-projected DOS were filtered out. A peak in the DOS was considered to be highly localized if a Gaussian fit exhibits an R^2 value of 0.9 or higher, has a base height (i.e. at the tails) that is less than 10% of the maximum value in the DOS, and exhibits a standard deviation less than 0.3 eV. To account for materials with asymmetric, spin-polarized DOS, we performed the aforementioned analysis separately for each spin channel where applicable. If at least one spin channel has a localized *d* state based on the aforementioned criteria, the materials was retained in the screening process. In this work, materials with localized *d* states were only considered if the peak maximum was located inside the valence band. Given the numerical fluctuations present in DFT-computed DOS, we acknowledge that this fitting approach is not perfect and will inevitably result in occasional misclassifications. Nonetheless, we found this approach to be sufficiently reliable for screening purposes.

Density of States Plots for Bulk Intermetallic Compounds

The DOS for the bulk structures plotted in Figure 1a and Figure 2c were obtained from the Materials Project and are based on PBE[6] calculations carried out in the Vienna *ab initio* Simulation Package[7–10] (`VASP`). The corresponding entries on the Materials Project are specified via their Materials Project IDs in the figure captions for ease-of-reference. For the periodic trend analyses in Figure 3 and Figures S7–S11, we chose

to recalculate the DOS for each bulk intermetallic compound using the Materials Project-compatible band structure workflow available in `Atomate`[11] v.1.0.3 and using `VASP` v.6.3.0. This is because some of the settings on the Materials Project have evolved over time (e.g. increased k-point density, use of `LMAXMIX` and `LASPH`), and we wanted to ensure the DOS were directly comparable. Additionally, many of the structures in Figure 3 and Figures S7–S11 were not previously available on the Materials Project.

Partial Charge Calculations

Bader charges[12–14] were computed via v.1.04 of the Henkelman group `bader` code. Voronoi deformation density (VDD) charges[15] were computed using `Critic2`[16] (commit 84692b2). Density-Derived Electrostatic and Chemical (DDEC6) charges[17,18] were computed via Chargemol v.09-26-2017. For the partial atomic charges of the bulk structures (e.g. Figure 2b), the charge densities were generated using the `MPStaticSet` settings in Atomate[11] and the DFT-optimized structures from the Materials Project. We recalculated the charge densities for each structure even for those with charge densities available on the Materials Project because some entries originally used the `ADDGRID` keyword in VASP, which we found can lead to erroneous partial atomic charges. If the absolute value of the sum of charges for a bulk material was found to be greater than 0.1, it was excluded from the partial charge analysis due to high numerical uncertainty (not uncommon with the VDD method in `Critic2`).

Surface and Adsorption Energy Calculations

Slab Generation and Adsorbate Placement

The initial geometry for the bulk structures were adopted from the Materials Project (v2021.11.10) using the Materials Project API.[3] The atomic positions and unit cell were re-relaxed using the same setting as the slab and slab–adsorbate calculations (see "Density Functional Theory Parameters" below). `Pymatgen` was then used to systematically construct surface slabs.[19] Each slab has a minimum height of 10 Å, minimum length and width of 8 Å, and minimum vacuum size of 20 Å. Atoms located 2 Å below the surface were fixed to mimic bulk constraints of the surface structure. For each bulk structure, unique low-miller index surfaces (up to a miller index of 1 in each dimension) were carved. Since some structures considered in this work have relatively low symmetry, a large number of unique surfaces can potentially be generated using this approach. For computational convenience, we selected a random subset of three generated slabs (except for the elemental structures for which we retained all such low miller-index slabs). For all calculations involving slab models, the cell shape and volume were kept fixed.

Using the adsorption site-finding method in `Pymatgen`,[20] adsorbates were placed in an atop adsorption mode on unique adsorption sites for each slab and allowed to relax along with the surface atoms. We chose to model CO adsorption in an atop configuration for the purpose of identifying how localized d states influence reactivity, although we acknowledge that this will not always be the minimum energy adsorption mode. We used the `CrystalNN`[21,22] algorithm in `Pymatgen` (with the porous correction disabled) to confirm that the adsorbate was still present in an atop position after the structure relaxation. To avoid generating structure–property relationships in rare cases of surface reconstruction, we used the `StructureMatcher` algorithm in `Pymatgen` to exclude materials where the slab is no longer considered to be the same before and after adsorbate binding.

Density Functional Theory Parameters

High-throughput DFT calculations for the surface and adsorption energy analysis were orchestrated using the Quantum Accelerator (`QuAcc`) v.0.0.3 code,[23] which is inspired by `Atomate2`[11] and built upon the Atomic Simulation Environment (`ASE`),[24] `Pymatgen`,[25] `Custodian`,[25] `Jobflow`, and `FireWorks`.[26] In analogy to prior work,[27] the automated workflow consists of a bulk structure relaxation, slab generation, slab structure relaxations (with fixed lattice constants), automated adsorbate placement, and subsequent geometry optimizations of the slab–adsorbate structures. For the DFT settings, we used `VASP` v.6.3.0, the RPBE functional,[28] a 450 eV plane-wave kinetic energy cutoff, and the `VASP`-recommended v.54 projector-augmented wave (PAW)[29,30] PBE[6] pseudopotentials. We chose to use RPBE as opposed to PBE for the

adsorption energy calculations since the former is known to be more accurate for CO chemisorption.[20,28,31] A Γ-centered k-point grid of $50\ \text{Å}/a\ \times 50\ \text{Å}/b \times 50\ \text{Å}/c$ was adopted for the bulk calculations with the number of k-points in each dimension rounded up to the next highest integer. For slab calculations, the same k-point mesh was used but with a single k-point in the c dimension (i.e. the dimension containing vacuum, as described below). The accurate-precision keyword was enabled in `VASP`, the self-consistent field (SCF) was converged to at least 10^{-5} eV, the forces were converged such that the magnitude of the maximum force is less than 0.03 eV/Å, and symmetry constraints were disabled during structure relaxations. By default, Gaussian smearing was used for structure relaxations with a smearing width of 0.05 eV. The tetrahedron method with Blöchl corrections[32] was used for single-point calculations since this is recommended for producing accurate DOS. For the DOS plots throughout this work, Gaussian broadening with a standard deviation of 0.1 eV was applied to smooth the otherwise jagged nature of the DOS when computed using the tetrahedron method. A dipole correction was applied in the vacuum dimension for the slab calculations.[33] The converged magnetic moments from the Materials Project were used as the initial guess for the RPBE structure relaxations carried out in this work where applicable.

Adsorption energies were calculated such that a more exothermic value is indicative of stronger binding and were calculated using the corresponding isolated gas-phase molecule for the reference-state. The adsorption energy of CO, ΔE_{CO}, was therefore calculated as

$$\Delta E_{\text{CO}} = E_{\text{CO}*} - \left(E_* + E_{\text{CO (g)}}\right) \tag{S1}$$

where E_{CO^*} is the energy of the slab–adsorbate system, E_* is the energy of the adsorbate-free slab, and $E_{\text{CO (g)}}$ is the energy of a single, isolated CO molecule in a box with ~20 Å of vacuum space in each dimension.

Definitions of the Density of States Features

The d-band center, ε_d, was calculated as the first power moment given by

$$\varepsilon_d = \frac{\int_{-\infty}^{\infty} \rho_d(\varepsilon)\varepsilon\, d\varepsilon}{\int_{-\infty}^{\infty} \rho_d(\varepsilon)\, d\varepsilon} \tag{S2}$$

where ε is the energy (with respect to the Fermi level), and ρ_d is the d-projected density of states. The d-band width, W_d, was calculated as

$$W_d = \left(\frac{\int_{-\infty}^{\infty} \rho(\varepsilon)(\varepsilon - \varepsilon_d)^2\, d\varepsilon}{\int_{-\infty}^{\infty} \rho(\varepsilon)\ d\varepsilon}\right)^{\frac{1}{2}} \tag{S3}$$

The d-band upper edge, ε_u, was calculated either via the definition of Xin et al.[34] or Vojvodic et al.[35] given as

$$\varepsilon_{u,\text{Xin}} = \underset{\varepsilon}{\text{argmax}} \frac{1}{\pi} P \int_{-\infty}^{\infty} \frac{\rho(\varepsilon')}{\varepsilon - \varepsilon'} d\varepsilon' \tag{S4}$$

where P is principal value of the integral and

$$\varepsilon_{u,\text{Vojvodic}} = \varepsilon_d + \frac{W_d}{2} \tag{S5}$$

respectively. These properties have since been added to `Pymatgen` as of v2022.3.24.

Materials Selection for Surface and Adsorption Energy Calculations

For the surface relaxations and adsorption energy calculations, we selected intermetallics with localized *d* states on Rh, Ir, Pd, Pt, and Cu based on the screening process shown in Figure 1. To reduce the computational burden, structures with magnetic character were not considered for this analysis. We also omitted surface and CO adsorption calculations for any materials where the *d*-projected DOS of the surface site was predicted to have a larger *d*-band width than the elemental reference surface despite the bulk *d*-band of the former being comparatively narrow. This occurred for the Cu binding sites of $CuMPd_2$ (M = Al, Zn, Ga, In). At the end of the screening procedure, a total of 195 unique DFT-optimized intermetallic surface slabs with corresponding CO adsorption energies were calculated. The remaining structures did not complete within the pre-specified 48-hour wall-time or had an error that could not be automatically corrected using `Custodian`.

Modified Newns-Anderson Model

The hybridization energy, E_{hyb}, the orthogonalization energy, E_{ortho}, and the chemisorption energy, $\Delta E_{\mathrm{chemi}}$, are all generated through the method described by Vijay and coworkers.[36] In this section, we briefly describe the method as well as the input quantities needed from the DFT calculations.

$\Delta E_{\mathrm{chemi}}$ is broken down as the sum of two components,

$$\Delta E_{\mathrm{chemi}}(\epsilon_d, w_d) = E_{\mathrm{hyb}}(\epsilon_d, w_d) + E_{\mathrm{ortho}}(\epsilon_d, w_d) \tag{S6}$$

where ϵ_d and w_d are the *d*-band center and *d*-band width, respectively. $E_{\mathrm{hyb}}(\epsilon_d, w_d)$ is given by a modified form of the Newns-Anderson expressions,

$$E_{\mathrm{hyb}}(\epsilon_d, w_d) = \frac{2}{\pi}\int_{-\infty}^{\epsilon_{\mathrm{f}}} \arctan\left(\frac{\Delta_d + \Delta_0}{\epsilon - \epsilon_a - \Lambda}\right) d\epsilon - 2\epsilon_a \tag{S7}$$

where Δ_d is a continuous coupling element between the *d*-states of the metal to which the adsorbate is bound and the states of the adsorbate, Δ_0 is an augmentation (to the adsorbate density of states) due to the *sp*-density of states of the metal, ϵ_a is the re-normalized energy level of the adsorbate, Λ is the Hilbert transform of Δ_d, and ϵ_{f} is location of the Fermi level.

The orthogonalization energy is given by,

$$E_{\mathrm{ortho}}(\epsilon_d, w_d) = -2(n_a + f)V_{ak} \tag{S8}$$

where V_{ak} is the effective coupling matrix element, f is the fractional filling of the metal density of states given by

$$f = \int_{-\infty}^{\epsilon_{\mathrm{f}}} \Delta_d \,, \tag{S9}$$

and n_a is the occupancy of the adsorbate comes from the adsorbate density of states ρ_{aa} given by

$$n_a = \int_{-\infty}^{\epsilon_{\mathrm{f}}} \rho_{aa} \tag{S10}$$

where

$$\rho_{aa}(\epsilon) = \pi^{-1}\frac{\Delta_d + \Delta_0}{[\epsilon - \epsilon_a - \Lambda]^2 + (\Delta_d + \Delta_0)^2}. \tag{S11}$$

Throughout this work, we use Δ_d directly from the DFT-calculated *d*-projected density of states of the binding site on the bare elemental or intermetallic surface, ρ_d, such that

$$\Delta_d = \pi V_{ak}^2 \rho_d. \quad \text{(S12)}$$

Since ρ_d is on a numerical grid, all quantities used in the computations and their associated integrals are computed numerically using `numpy.trapz`.[37]

Model Parameters for CO Adsorption in the Modified Newns-Anderson Model

In this work, we use the Blyholder model[38] to understand CO chemisorption within the framework listed above.[39] The two most relevant electronic states are assumed to be the $2\pi^*$ state and the 5σ state. For each adsorbate state (5σ and $2\pi^*$), we fit $\alpha = S_{ak}/V_{ak}$ and $\beta = V_{ak}^2/V_{sd}^2$, where V_{sd} is taken from tabulated values, corresponding to the bulk metal, in Ref. [36]. To reduce the number of fitting parameters, we assume that $S_{5\sigma}/S_{2\pi} = V_{5\sigma}/V_{2\pi} = \kappa$, where κ is a separate fitting parameter. Further, we assume a constant the *sp*-augmentation (i.e. $\Delta_0 = 0.1$ eV).[36,39] The model parameters are shown in Table S1, and the results of the model fitting procedure are shown in Figure S1.

Table S1. Model parameters for the modified Newns–Anderson model of CO chemisorption.

State	ϵ_a (eV)	α (eV^{-1})	β (eV^2)	Δ_0 (eV)
$\epsilon_{5\sigma}$	–7	0.051	2.96	0.1
$\epsilon_{2\pi^*}$	2.5	0.046	2.66	0.1

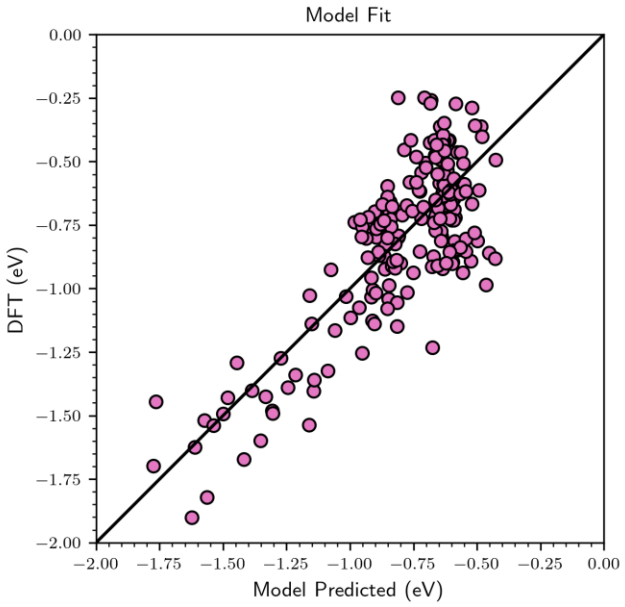

Figure S1. Comparison of the DFT-computed CO adsorption energy and the model-predicted energy (*x*-axis) for the intermetallics with localized *d* states. The mean absolute error is 0.16 eV and $R^2 = 0.65$.

The data in Figure 5 is generated by representing the *d*-projected density of states as a semi-ellipse,

$$\rho_d = \left(1 - \left(\frac{\epsilon - \epsilon_d}{w_d}\right)^2\right)^{\frac{1}{2}} \quad \text{(S13)}$$

where ρ_d is fit to the *d*-projected density of states through the fitting parameters ϵ_d and w_d. The contour map in Figure 5 is generated by passing $\rho_d(\epsilon_d, w_d)$ to Equation S7.

Additional Results

Metals with Localized *d* States: Partial Charges

As shown in Figure S2, the majority of the atoms with localized *d* states have anionic character. This is true across the Bader, VDD, and DDEC6 charge partitioning schemes. It is important to note that the large magnitudes observed with the Bader method are a known limitation of the method,[15,40] and qualitative trends are likely more informative than quantitative values. We consider it unlikely that the metals considered in this work have oxidation states at or below –2 in practice. VDD charges were made to correct for this limitation of the Bader method,[15] which explains the smaller magnitudes on average. However, VDD charges are often lower than virtually all other charge assignment methods[40] so are likely an underprediction in terms of the magnitude of charge transfer. DDEC6 charges are arguably some of the most reliable to-date,[40] and we find that anionic character is present for many of the localized *d* states using this method as well. The distribution of partial atomic charges for the atoms with localized *d* states broken down by element is shown in Figure 2b and Figure S3.

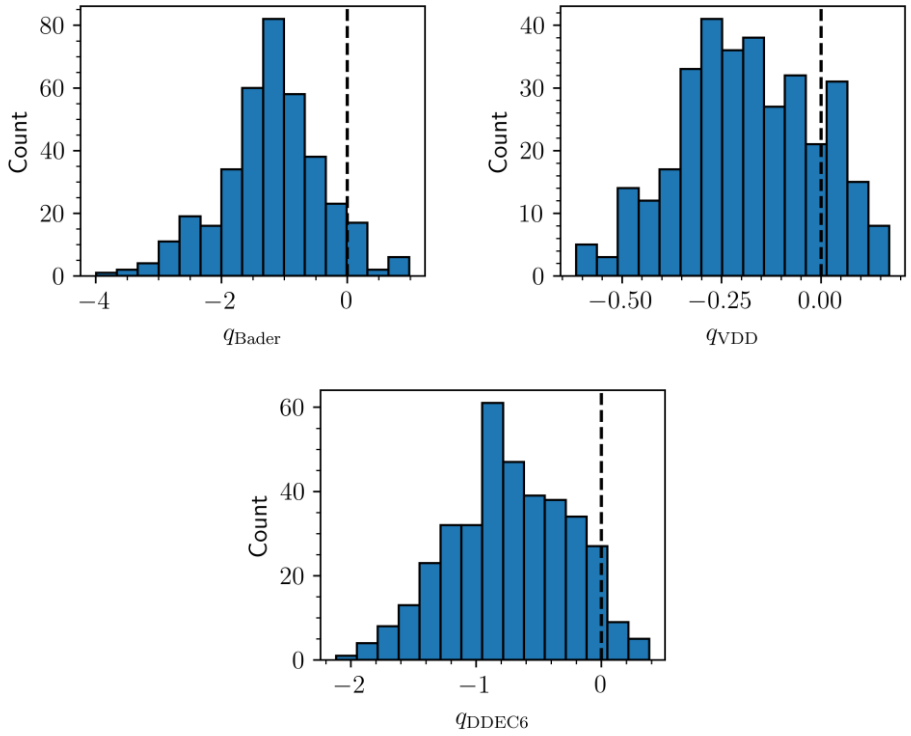

Figure S2. Histograms of the Bader partial atomic charges, q_{Bader}, DDEC6 partial atomic charges, q_{DDEC6}, and Voronoi deformation density (VDD) partial atomic charges, q_{VDD}, for the metals with localized *d* states identified in the screening process. A negative value implies anionic character, whereas a positive value implies cationic character. The bulk structures were used for the partial charge calculations.

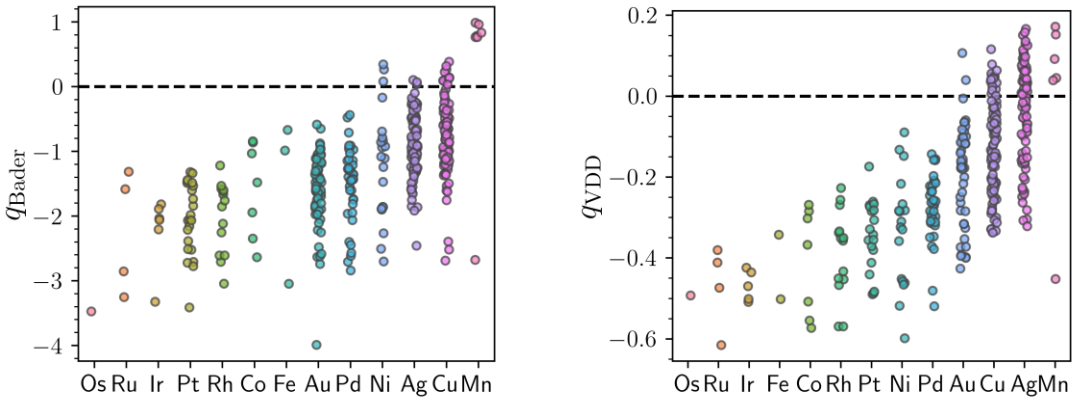

Figure S3. Distribution of the Bader partial atomic charges and Voronoi deformation density (VDD) partial atomic charges, q_{VDD}, for the metals with localized *d* states identified in the screening process. The points are jittered horizontally for ease of visualization. The bulk structures were used for the partial charge calculations.

Metals with Localized *d* States: Structure and Composition

The distribution of transition metals with localized *d* states from the screening process is shown in Figure S4. Late transition metals, in particular those of groups 10 and 11, are the most common across the dataset. The surrounding metals in the crystal structures with localized *d* states are summarized in Figure S5 for the binary intermetallics and Figure S6 for the ternary intermetallics and higher. These elements span most of the periodic table, but groups 1–3 are particularly common.

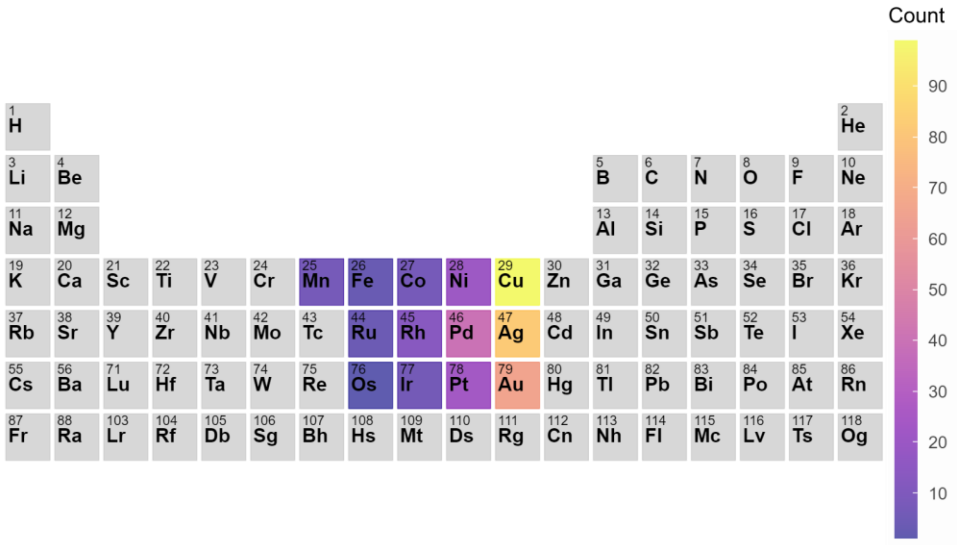

Figure S4. Distribution of transition metal elements with localized *d* states based on the screening process shown in Figure 1b. Note that only group 3–11 metals were considered for the localized *d* state screening process.

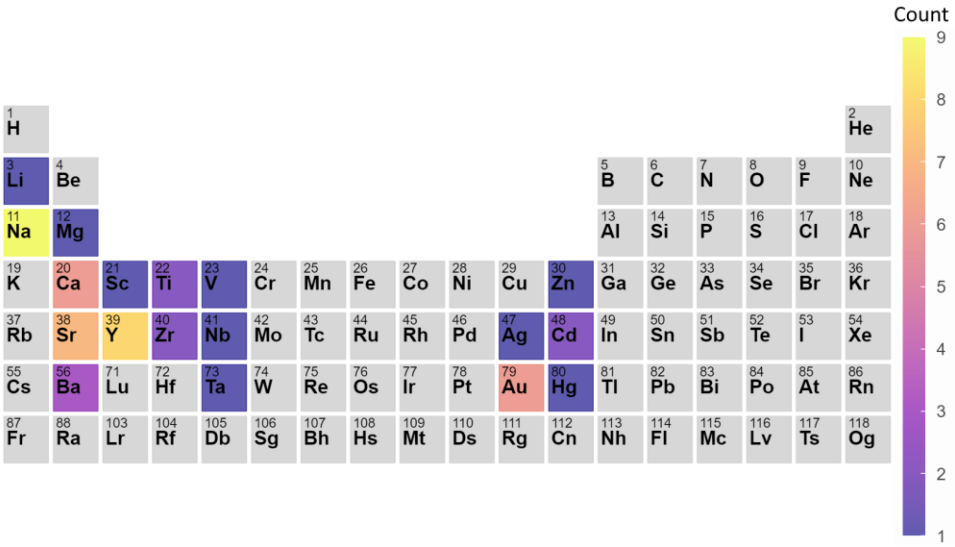

Figure S5. Distribution of metals on the present in the binary intermetallics with localized *d* state transition metals based on the screening process shown in Figure 1b, excluding those already included in Figure S4.

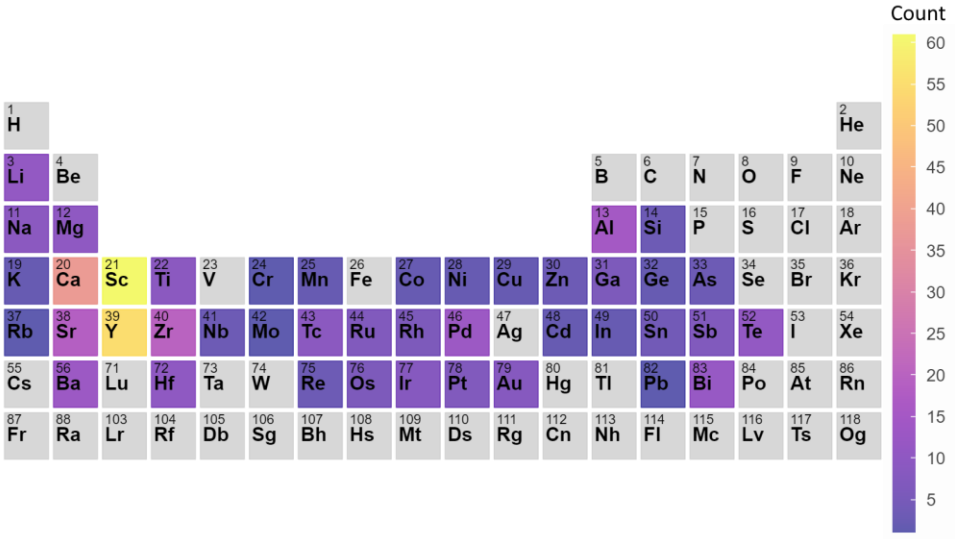

Figure S6. Distribution of metals present in the ternary and higher-composition intermetallics with localized *d* state transition metals based on the screening process shown in Figure 1b, excluding those already included in Figure S4.

Periodic Trends for Select Systems

The *d*-projected DOS for atom X in Na_3X, Y_3X, Ag_3X, and Au_3X are shown in Figures S7–S10 (as a complement to Figure 3). Spin-unrestricted DOS are shown for Ag_3X (X = Mn, Fe, Co, Ni, Cu) in Figure S11. Although Ag_3X (X = Co, Fe, Mn) are predicted to have magnetic character as shown in Figure 3, the analysis in Figure S11 shows that the trend of increasing *d*-band center with decreasing group number is robust when spin-polarization is not present.

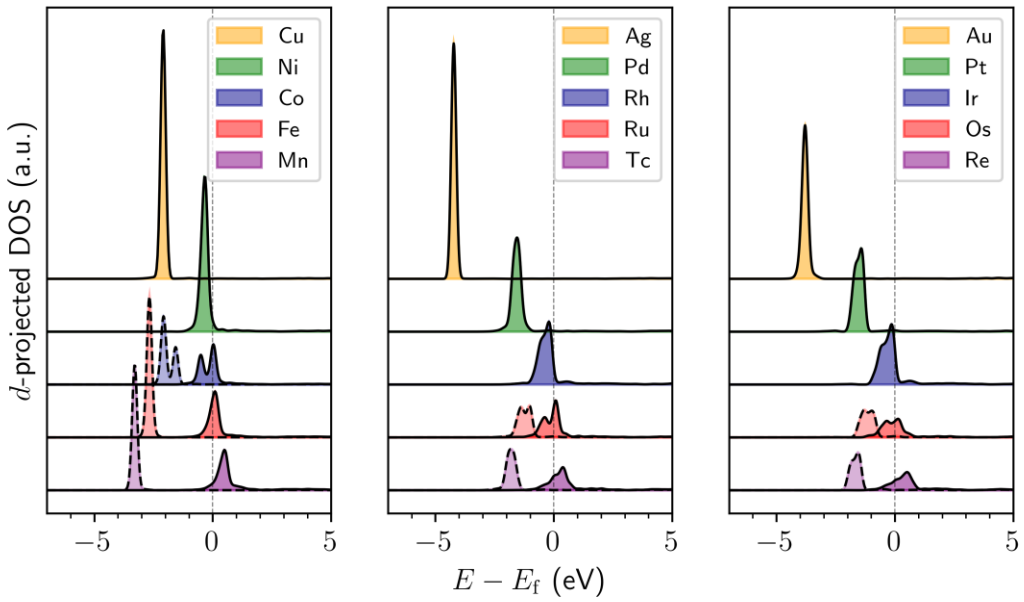

Figure S7. *d*-projected DOS for atom X in bulk, cubic Na_3X (X = Mn, Fe, Co, Ni, Cu; Tc, Ru, Rh, Pd, Ag; Re, Os, Ir, Pt, Au). In the case of magnetic structures, the dashed and solid lines distinguish between the spin-up and spin-down channels. Energies, E, are shown with respect to the Fermi level, E_f.

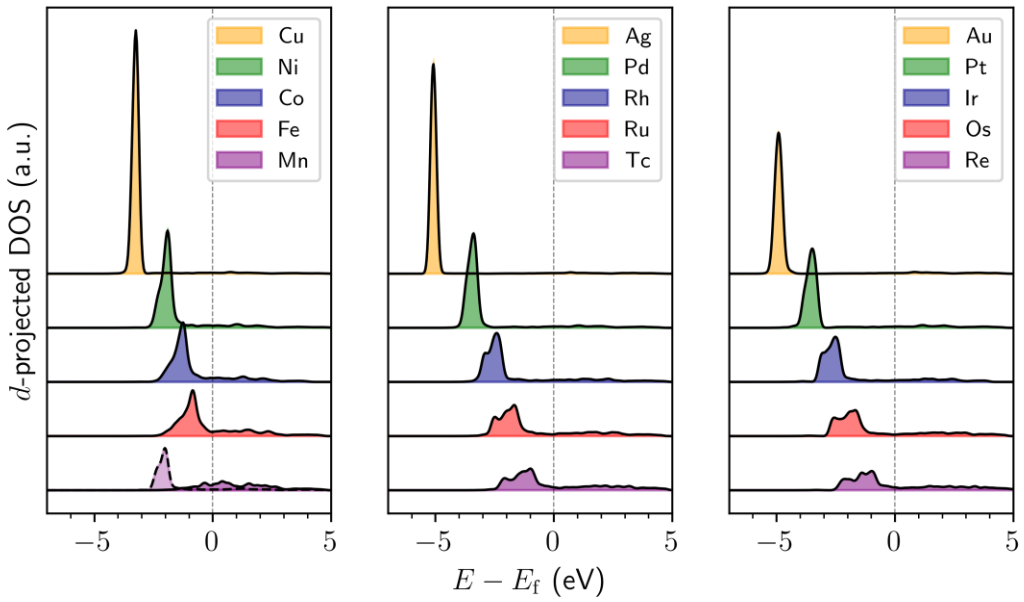

Figure S8. *d*-projected DOS for atom X in bulk, orthorhombic Y_3X (X = Mn, Fe, Co, Ni, Cu; Tc, Ru, Rh, Pd, Ag; Re, Os, Ir, Pt, Au). In the case of magnetic structures, the dashed and solid lines distinguish between the spin-up and spin-down channels. Energies, E, are shown with respect to the Fermi level, E_f.

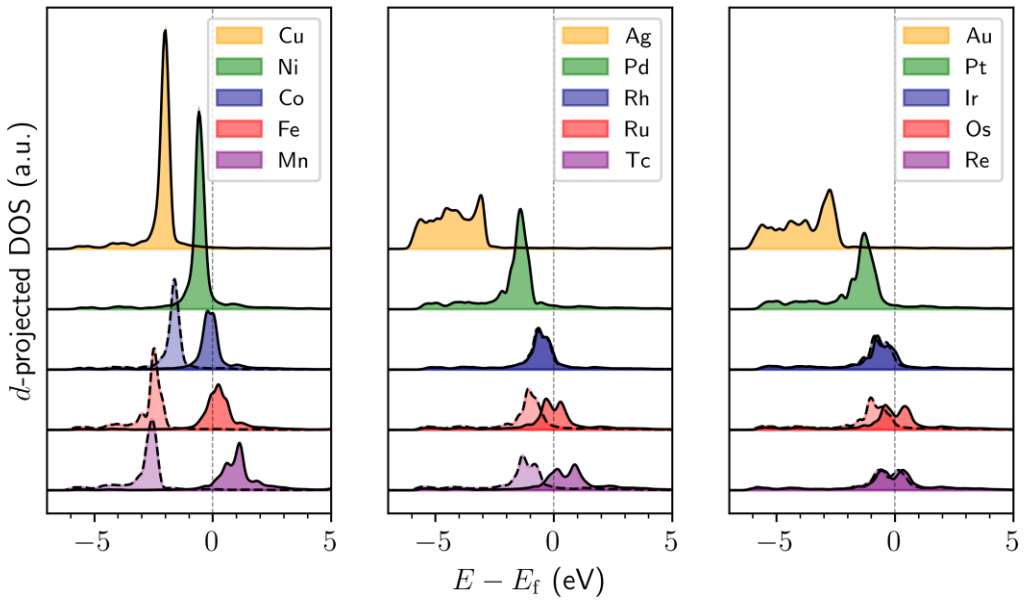

Figure S9. *d*-projected DOS for atom X in bulk, hexagonal Ag_3X (X = Mn, Fe, Co, Ni, Cu; Tc, Ru, Rh, Pd, Ag; Re, Os, Ir, Pt, Au). In the case of magnetic structures, the dashed and solid lines distinguish between the spin-up and spin-down channels. Energies, E, are shown with respect to the Fermi level, E_f.

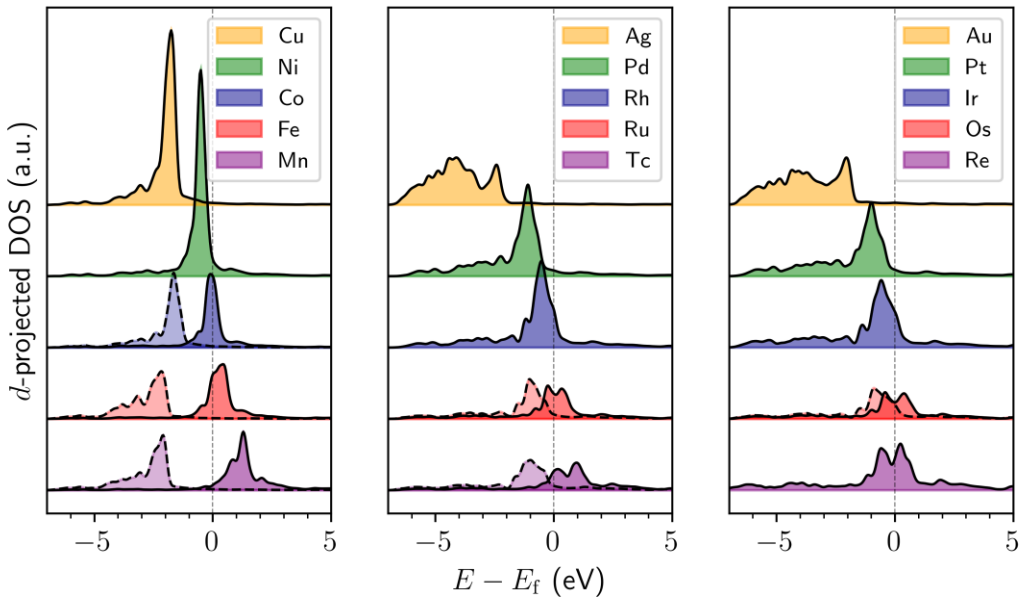

Figure S10. *d*-projected DOS for atom X in bulk, hexagonal Au_3X (X = Mn, Fe, Co, Ni, Cu; Tc, Ru, Rh, Pd, Ag; Re, Os, Ir, Pt, Au). In the case of magnetic structures, the dashed and solid lines distinguish between the spin-up and spin-down channels. Energies, E, are shown with respect to the Fermi level, E_f.

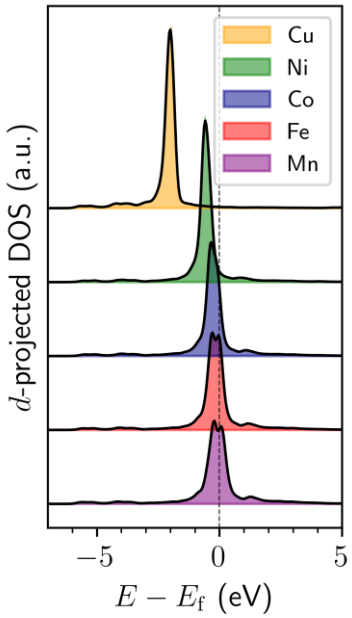

Figure S11. Spin-restricted *d*-projected DOS for atom X in bulk, hexagonal Ag_3X (X = Mn, Fe, Co, Ni, Cu). Energies, E, are shown with respect to the Fermi level, E_f.

d-band Trends Between the Bulk and Surface

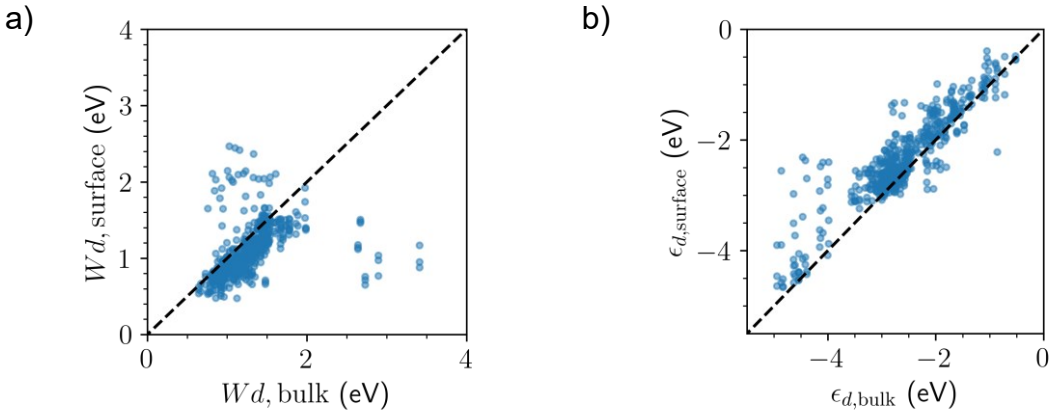

Figure S12. a) *d*-band widths for the surface atoms with localized *d* states as a function of the corresponding *d*-band widths in the bulk structure. b) *d*-band centers for the surface atoms with localized *d* states as a function of the corresponding *d*-band centers in the bulk structure.

d-band Trends Between the Intermetallics and Elementals

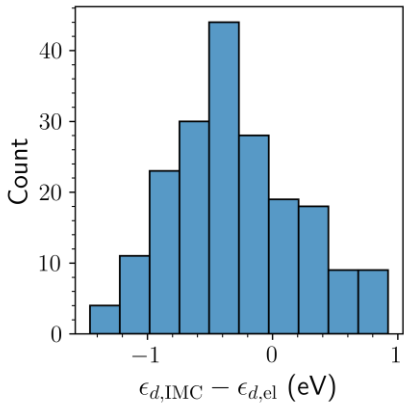

Figure S13. Histogram of the difference in *d*-band centers for the localized *d* state metal of the intermetallic surfaces, $\varepsilon_{d,\mathrm{IMC}}$, compared to their elemental surfaces, $\varepsilon_{d,\mathrm{el}}$. A positive value indicates a higher *d*-band center in the intermetallic compared to the elemental analogue and vice versa. The values for the elemental analogues are averaged across the various surfaces considered in this work. The site-projected *d*-band for the metal acting as the CO binding site is used.

Charge on the CO Adsorbate

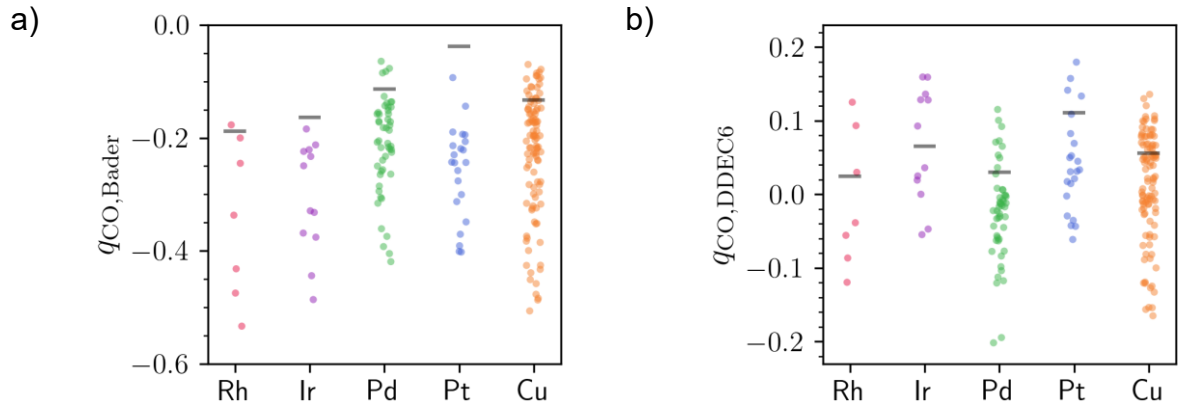

Figure S14. a) Sum of Bader charges on the CO adsorbate, $q_{\mathrm{CO,Bader}}$, and b) Sum of DDEC6 charges on the CO adsorbate, $q_{\mathrm{CO,DDEC6}}$, for various surfaces with localized *d* states on the specified metal sites. Each point represents a different composition and/or surface facet. The points are jittered horizontally for ease-of-visualization. The dashed, horizontal lines represent the average ΔE_{CO} value for the (100), (110), and (111) surfaces of the corresponding ground-state, elemental reference structure. The sign convention is such that a negative value implies partial reduction and vice versa.

CO Adsorption Trends

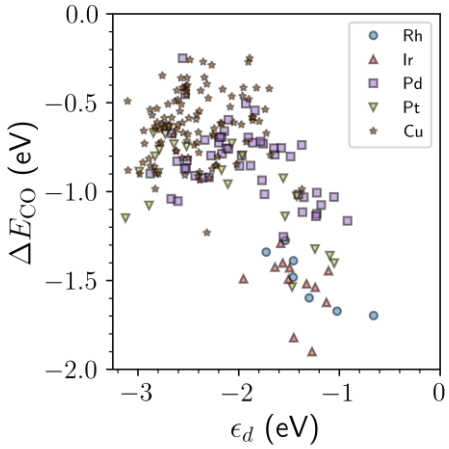

Figure S15. CO adsorption energy, ΔE_{CO}, plotted as a function of the site-projected *d*-band center, ε_d, at the metal binding sites with localized *d*-states of the intermetallic compounds. A linear fit has an R^2 and mean absolute error of 0.32 and 0.22 eV, respectively.

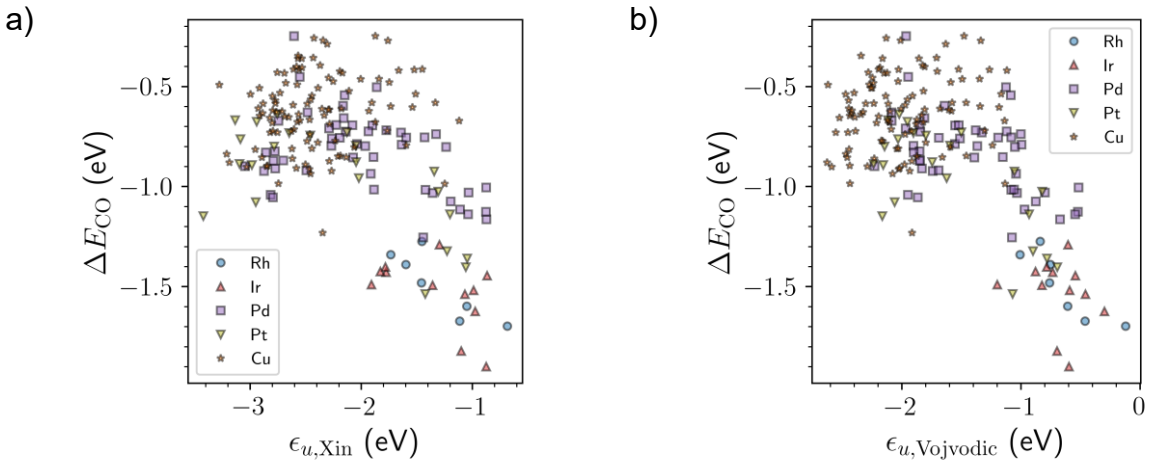

Figure S16. a) CO adsorption energy, ΔE_{CO}, plotted as a function of the site-projected *d*-band upper edge descriptor, $\varepsilon_{u,Xin}$, at the metal binding sites with localized *d*-states of the intermetallic compounds based on the Hilbert transform. A linear fit has an R^2 and mean absolute error of 0.26 and 0.22 eV, respectively. b) CO adsorption energy, ΔE_{CO}, plotted as a function of the site-projected *d*-band upper edge descriptor, $\varepsilon_{u,Vojvodic}$, at the metal binding sites with localized *d*-states of the intermetallic compounds based on the semi-elliptical model. A linear fit has an R^2 and mean absolute error of 0.39 and 0.20 eV, respectively.

Supporting References

(1) Draxl, C.; Scheffler, M. NOMAD: The FAIR Concept for Big Data-Driven Materials Science. *MRS Bull* 2018, *43* (9), 676–682. https://doi.org/10.1557/mrs.2018.208.
(2) Draxl, C.; Scheffler, M. The NOMAD Laboratory: From Data Sharing to Artificial Intelligence. *J Phys Mater* 2019, *2* (3), 036001. https://doi.org/10.1088/2515-7639/ab13bb.
(3) Ong, S. P.; Cholia, S.; Jain, A.; Brafman, M.; Gunter, D.; Ceder, G.; Persson, K. A. The Materials Application Programming Interface (API): A Simple, Flexible and Efficient API for Materials Data Based on REpresentational State Transfer (REST) Principles. *Comp Mater Sci* 2015, *97*, 209–215. https://doi.org/10.1016/j.commatsci.2014.10.037.
(4) Woods-Robinson, R.; Horton, M. K.; Persson, K. A. A Method to Computationally Screen for Tunable Properties of Crystalline Alloys. *arXiv* 2022. https://doi.org/10.48550/arXiv.2206.10715.
(5) Virtanen, P.; Gommers, R.; Oliphant, T. E.; Haberland, M.; Reddy, T.; Cournapeau, D.; Burovski, E.; Peterson, P.; Weckesser, W.; Bright, J.; Walt, S. J. van der; Brett, M.; Wilson, J.; Millman, K. J.; Mayorov, N.; Nelson, A. R. J.; Jones, E.; Kern, R.; Larson, E.; Carey, C. J.; Polat, İ.; Feng, Y.; Moore, E. W.; VanderPlas, J.; Laxalde, D.; Perktold, J.; Cimrman, R.; Henriksen, I.; Quintero, E. A.; Harris, C. R.; Archibald, A. M.; Ribeiro, A. H.; Pedregosa, F.; Mulbregt, P. van; Contributors, S. 1 0; Vijaykumar, A.; Bardelli, A. P.; Rothberg, A.; Hilboll, A.; Kloeckner, A.; Scopatz, A.; Lee, A.; Rokem, A.; Woods, C. N.; Fulton, C.; Masson, C.; Häggström, C.; Fitzgerald, C.; Nicholson, D. A.; Hagen, D. R.; Pasechnik, D. V.; Olivetti, E.; Martin, E.; Wieser, E.; Silva, F.; Lenders, F.; Wilhelm, F.; Young, G.; Price, G. A.; Ingold, G.-L.; Allen, G. E.; Lee, G. R.; Audren, H.; Probst, I.; Dietrich, J. P.; Silterra, J.; Webber, J. T.; Slavič, J.; Nothman, J.; Buchner, J.; Kulick, J.; Schönberger, J. L.; Cardoso, J. V. de M.; Reimer, J.; Harrington, J.; Rodríguez, J. L. C.; Nunez-Iglesias, J.; Kuczynski, J.; Tritz, K.; Thoma, M.; Newville, M.; Kümmerer, M.; Bolingbroke, M.; Tartre, M.; Pak, M.; Smith, N. J.; Nowaczyk, N.; Shebanov, N.; Pavlyk, O.; Brodtkorb, P. A.; Lee, P.; McGibbon, R. T.; Feldbauer, R.; Lewis, S.; Tygier, S.; Sievert, S.; Vigna, S.; Peterson, S.; More, S.; Pudlik, T.; Oshima, T.; Pingel, T. J.; Robitaille, T. P.; Spura, T.; Jones, T. R.; Cera, T.; Leslie, T.; Zito, T.; Krauss, T.; Upadhyay, U.; Halchenko, Y. O.; Vázquez-Baeza, Y. SciPy 1.0: Fundamental Algorithms for Scientific Computing in Python. *Nat Methods* 2020, *17* (3), 261–272. https://doi.org/10.1038/s41592-019-0686-2.
(6) Perdew, J. P.; Burke, K.; Ernzerhof, M. Generalized Gradient Approximation Made Simple. *Phys Rev Lett* 1996, *77* (18), 3865–3868. https://doi.org/10.1103/physrevlett.77.3865.
(7) Kresse, G.; Hafner, J. Ab Initio Molecular Dynamics for Liquid Metals. *Phys Rev B* 1993, *47* (1), 558–561. https://doi.org/10.1103/physrevb.47.558.
(8) Kresse, G.; Hafner, J. Ab Initio Molecular-Dynamics Simulation of the Liquid-Metal–Amorphous-Semiconductor Transition in Germanium. *Phys Rev B* 1994, *49* (20), 14251–14269. https://doi.org/10.1103/physrevb.49.14251.
(9) Kresse, G.; Furthmüller, J. Efficiency of Ab-Initio Total Energy Calculations for Metals and Semiconductors Using a Plane-Wave Basis Set. *Comp Mater Sci* 1996, *6* (1), 15–50. https://doi.org/10.1016/0927-0256(96)00008-0.
(10) Kresse, G.; Furthmüller, J. Efficient Iterative Schemes for Ab Initio Total-Energy Calculations Using a Plane-Wave Basis Set. *Phys Rev B* 1996, *54* (16), 11169–11186. https://doi.org/10.1103/physrevb.54.11169.
(11) Mathew, K.; Montoya, J. H.; Faghaninia, A.; Dwarakanath, S.; Aykol, M.; Tang, H.; Chu, I.; Smidt, T.; Bocklund, B.; Horton, M.; Dagdelen, J.; Wood, B.; Liu, Z.-K.; Neaton, J.; Ong, S. P.; Persson, K.; Jain, A. Atomate: A High-Level Interface to Generate, Execute, and Analyze Computational Materials Science Workflows. *Comp Mater Sci* 2017, *139*, 140–152. https://doi.org/10.1016/j.commatsci.2017.07.030.
(12) Henkelman, G.; Arnaldsson, A.; Jónsson, H. A Fast and Robust Algorithm for Bader Decomposition of Charge Density. *Comp Mater Sci* 2006, *36* (3), 354–360. https://doi.org/10.1016/j.commatsci.2005.04.010.

(13) Sanville, E.; Kenny, S. D.; Smith, R.; Henkelman, G. Improved Grid-based Algorithm for Bader Charge Allocation. *J Comput Chem* 2007, *28* (5), 899–908. https://doi.org/10.1002/jcc.20575.
(14) Tang, W.; Sanville, E.; Henkelman, G. A Grid-Based Bader Analysis Algorithm without Lattice Bias. *J Phys Condens Matter* 2009, *21* (8), 084204. https://doi.org/10.1088/0953-8984/21/8/084204.
(15) Guerra, C. F.; Handgraaf, J.; Baerends, E. J.; Bickelhaupt, F. M. Voronoi Deformation Density (VDD) Charges: Assessment of the Mulliken, Bader, Hirshfeld, Weinhold, and VDD Methods for Charge Analysis. *J Comput Chem* 2004, *25* (2), 189–210. https://doi.org/10.1002/jcc.10351.
(16) Otero-de-la-Roza, A.; Johnson, E. R.; Luaña, V. Critic2: A Program for Real-Space Analysis of Quantum Chemical Interactions in Solids. *Comput Phys Commun* 2014, *185* (3), 1007–1018. https://doi.org/10.1016/j.cpc.2013.10.026.
(17) Manz, T. A.; Limas, N. G. Introducing DDEC6 Atomic Population Analysis: Part 1. Charge Partitioning Theory and Methodology. *RSC Adv* 2016, *6* (53), 47771–47801. https://doi.org/10.1039/c6ra04656h.
(18) Limas, N. G.; Manz, T. A. Introducing DDEC6 Atomic Population Analysis: Part 2. Computed Results for a Wide Range of Periodic and Nonperiodic Materials. *RSC Adv* 2016, *6* (51), 45727–45747. https://doi.org/10.1039/c6ra05507a.
(19) Sun, W.; Ceder, G. Efficient Creation and Convergence of Surface Slabs. *Surf Sci* 2013, *617*, 53–59. https://doi.org/10.1016/j.susc.2013.05.016.
(20) Montoya, J. H.; Persson, K. A. A High-Throughput Framework for Determining Adsorption Energies on Solid Surfaces. n*pj Comput Mater* 2017, *3* (1), 14. https://doi.org/10.1038/s41524-017-0017-z.
(21) Zimmermann, N. E. R.; Jain, A. Local Structure Order Parameters and Site Fingerprints for Quantification of Coordination Environment and Crystal Structure Similarity. *RSC Adv* 2020, *10* (10), 6063–6081. https://doi.org/10.1039/c9ra07755c.
(22) Pan, H.; Ganose, A. M.; Horton, M.; Aykol, M.; Persson, K. A.; Zimmermann, N. E. R.; Jain, A. Benchmarking Coordination Number Prediction Algorithms on Inorganic Crystal Structures. *Inorg Chem* 2021, *60* (3), 1590–1603. https://doi.org/10.1021/acs.inorgchem.0c02996.
(23) Rosen, A. S. *QuAcc – The Quantum Accelerator*. https://github.com/arosen93/quacc.
(24) Larsen, A. H.; Mortensen, J. J.; Blomqvist, J.; Castelli, I. E.; Christensen, R.; Dułak, M.; Friis, J.; Groves, M. N.; Hammer, B.; Hargus, C.; Hermes, E. D.; Jennings, P. C.; Jensen, P. B.; Kermode, J.; Kitchin, J. R.; Kolsbjerg, E. L.; Kubal, J.; Kaasbjerg, K.; Lysgaard, S.; Maronsson, J. B.; Maxson, T.; Olsen, T.; Pastewka, L.; Peterson, A.; Rostgaard, C.; Schiøtz, J.; Schütt, O.; Strange, M.; Thygesen, K. S.; Vegge, T.; Vilhelmsen, L.; Walter, M.; Zeng, Z.; Jacobsen, K. W. The Atomic Simulation Environment—a Python Library for Working with Atoms. *J Phys Condens Matter* 2017, *29* (27), 273002. https://doi.org/10.1088/1361-648x/aa680e.
(25) Ong, S. P.; Richards, W. D.; Jain, A.; Hautier, G.; Kocher, M.; Cholia, S.; Gunter, D.; Chevrier, V. L.; Persson, K. A.; Ceder, G. Python Materials Genomics (Pymatgen): A Robust, Open-Source Python Library for Materials Analysis. *Comp Mater Sci* 2013, *68*, 314–319. https://doi.org/10.1016/j.commatsci.2012.10.028.
(26) Jain, A.; Ong, S. P.; Chen, W.; Medasani, B.; Qu, X.; Kocher, M.; Brafman, M.; Petretto, G.; Rignanese, G.; Hautier, G.; Gunter, D.; Persson, K. A. FireWorks: A Dynamic Workflow System Designed for High-throughput Applications. *Concurrency Comput Pract Exp* 2015, *27* (17), 5037–5059. https://doi.org/10.1002/cpe.3505.
(27) Andriuc, O.; Siron, M.; Montoya, J. H.; Horton, M.; Persson, K. A. Automated Adsorption Workflow for Semiconductor Surfaces and the Application to Zinc Telluride. *J Chem Inf Model* 2021, *61* (8), 3908–3916. https://doi.org/10.1021/acs.jcim.1c00340.
(28) Hammer, B.; Hansen, L. B.; Nørskov, J. K. Improved Adsorption Energetics within Density-Functional Theory Using Revised Perdew-Burke-Ernzerhof Functionals. *Phys Rev B* 1999, *59* (11), 7413–7421. https://doi.org/10.1103/physrevb.59.7413.
(29) Blöchl, P. E. Projector Augmented-Wave Method. *Phys Rev B* 1994, *50* (24), 17953–17979. https://doi.org/10.1103/physrevb.50.17953.

(30) Kresse, G.; Joubert, D. From Ultrasoft Pseudopotentials to the Projector Augmented-Wave Method. *Phys Rev B* 1998, *59* (3), 1758–1775. https://doi.org/10.1103/physrevb.59.1758.
(31) Abild-Pedersen, F.; Andersson, M. P. CO Adsorption Energies on Metals with Correction for High Coordination Adsorption Sites – A Density Functional Study. *Surf Sci* 2007, *601* (7), 1747–1753. https://doi.org/10.1016/j.susc.2007.01.052.
(32) Blöchl, P. E.; Jepsen, O.; Andersen, O. K. Improved Tetrahedron Method for Brillouin-Zone Integrations. *Phys Rev B* 1994, *49* (23), 16223–16233. https://doi.org/10.1103/physrevb.49.16223.
(33) Toriyama, M. Y.; Ganose, A. M.; Dylla, M.; Anand, S.; Park, J.; Brod, M. K.; Munro, J. M.; Persson, K. A.; Jain, A.; Snyder, G. J. How to Analyse a Density of States. *Mater Today Electron* 2022, *1*, 100002. https://doi.org/10.1016/j.mtelec.2022.100002.
(34) Xin, H.; Vojvodic, A.; Voss, J.; Nørskov, J. K.; Abild-Pedersen, F. Effects of D-Band Shape on the Surface Reactivity of Transition-Metal Alloys. *Phys Rev B* 2014, *89* (11), 115114. https://doi.org/10.1103/physrevb.89.115114.
(35) Vojvodic, A.; Nørskov, J. K.; Abild-Pedersen, F. Electronic Structure Effects in Transition Metal Surface Chemistry. *Top Catal* 2014, *57* (1–4), 25–32. https://doi.org/10.1007/s11244-013-0159-2.
(36) Vijay, S.; Kastlunger, G.; Chan, K.; Nørskov, J. K. Limits to Scaling Relations between Adsorption Energies? *J Chem Phys* 2022, *156* (23), 231102. https://doi.org/10.1063/5.0096625.
(37) Harris, C. R.; Millman, K. J.; Walt, S. J. van der; Gommers, R.; Virtanen, P.; Cournapeau, D.; Wieser, E.; Taylor, J.; Berg, S.; Smith, N. J.; Kern, R.; Picus, M.; Hoyer, S.; Kerkwijk, M. H. van; Brett, M.; Haldane, A.; Río, J. F. del; Wiebe, M.; Peterson, P.; Gérard-Marchant, P.; Sheppard, K.; Reddy, T.; Weckesser, W.; Abbasi, H.; Gohlke, C.; Oliphant, T. E. Array Programming with NumPy. *Nature* 2020, *585* (7825), 357–362. https://doi.org/10.1038/s41586-020-2649-2.
(38) Blyholder, G.; Allen, M. C. Infrared Spectra and Molecular Orbital Model for Carbon Monoxide Adsorbed on Metals. *J Am Chem Soc* 1969, *91* (12), 3158–3162. https://doi.org/10.1021/ja01040a009.
(39) Hammer, B.; Morikawa, Y.; Nørskov, J. K. CO Chemisorption at Metal Surfaces and Overlayers. *Phys Rev Lett* 1996, *76* (12), 2141–2144. https://doi.org/10.1103/physrevlett.76.2141.
(40) Manz, T. A. Seven Confluence Principles: A Case Study of Standardized Statistical Analysis for 26 Methods That Assign Net Atomic Charges in Molecules. *RSC Adv* 2020, *10* (72), 44121–44148. https://doi.org/10.1039/d0ra06392d.